Journal of Applied Physics

RESEARCH ARTICLE | SEPTEMBER 10 2026

Measuring the pre-heating zone thermal profile: Effect of thermal diffusivity on propagation in nanothermite composites

Keren Shi ; Yujie Wang ; Michael R. Zachariah

J. Appl. Phys. 140, 105904 (2026)
https://doi.org/10.1063/5.0341574

AIP Publishing

Journal of Applied Physics ARTICLE pubs.aip.org/aip/jap

Measuring the pre-heating zone thermal profile: Effect of thermal diffusivity on propagation in nanothermite composites

Cite as: J. Appl. Phys. **140**, 105904 (2026); doi: 10.1063/5.0341574
Submitted: 2 May 2026 · Accepted: 4 August 2026 ·
Published Online: 10 September 2026

Keren Shi, Yujie Wang, and Michael R. Zachariah[a)]

AFFILIATIONS

Department of Chemical and Environmental Engineering, University of California, Riverside, California 92521, USA

[a)]**Author to whom correspondence should be addressed:** mrz@engr.ucr.edu

ABSTRACT

The combustion behavior of nanothermite composites is governed by the coupled effects of chemical kinetics and transport (heat and mass). In this study, we investigated the role of thermal properties on the propagation of six nanothermite systems with distinct product morphologies. In particular, we manipulate the intrinsic thermal diffusivity by incorporating carbon fiber (CF). High-speed three-color imaging pyrometry combined with infrared thermography was employed to obtain complete temperature profiles during combustion extending from the pre-heating through the reaction zone. These data enabled us to extract in-operando thermal diffusivity via solution to the heat-equation. We find that while the CF, which is inert, did not alter the measured peak combustion temperature, it could be used to alter both the thermal diffusivity and propagation velocity. The nanothermite composites were classified based on the combustion product morphology observed by real-time imaging during combustion. Composites exhibiting dispersed phase products including Al/MnO_2, Ti/MnO_2, and B/Bi_2O_3, where CF intercepts ejected agglomerates and increases heat feedback to the pre-heating zone, thereby enhancing the burn rate. In contrast, for the composites with continuous phase products including B/MnO_2, B/Fe_2O_3, and B/Fe_3O_4, enhanced thermal diffusivity by CF increases energy dissipation from reaction zone, leading to reduced burn rate. Simulations reproduce the observed burn rate trends with CF addition, confirming that heat feedback plays a key role in the propagation of nanothermite composites. An in-operando methodology is developed to extract effective thermal diffusivity directly from experimentally measured combustion temperature profiles, enabling quantitative characterization of heat flux during combustion propagation.

I. INTRODUCTION

Nanothermite composites offer high energy density and reactivity by exploiting the reaction of nanoscale fuels and oxidizers.[1,2] After ignition, the combustion proceeds as a self-sustained wave governed by complex interaction of chemical kinetics, heat and mass transfer in the reaction, pre-heating, and product zones.[3,4] These regions can be conceptually distinguished from the steady-state temperature profile during combustion. The reaction zone is where exothermic reactions occur, and the temperature rapidly rises from the reaction initiation (ignition) temperature to the adiabatic flame temperature. In practice, the measured flame temperature is generally lower primarily due to heat losses and incomplete reaction resulting from particle agglomeration and reactive sintering. Upstream of this region lies the pre-heating zone, where heat conducted from the reaction front elevates the temperature from ambient to the reaction initiation temperature. Downstream is the product zone, where the temperature gradually decreases as thermal energy is dissipated to surroundings. Efforts to enhance combustion performance have focused on tailoring both reaction kinetics and heat transfer properties. Wang *et al.* investigated Al/CuO nanothermite laminates fabricated by direct writing and showed that decreasing bilayer thickness increases burn rate by shortening the oxygen diffusion distance.[5] Marín *et al.* enhanced reactivity in Al/CuO nanolaminates by incorporating a thin Cu interfacial layer, which promoted reactivity and burn rate by lowering the effective melting temperature of Al through Al/Cu alloy reaction.[6] Wang *et al.* used an unzipping polymer which generates low molecular weight fragments to reduce the nanoparticle agglomeration and result in burn rate and flame temperature increase.[7] Beyond modifying chemistry reactivity, studies

have demonstrated an important role of heat feedback in modulating propagation speed. Egan *et al.* examined different heat transfer mechanisms during combustion of nanothermite composites numerically and suggested that conduction, convection and radiation may not provide enough heat feedback for reaction propagation and the movement of condensed phase material should be considered in future models.[8] This hypothesis was tested when small amount of CuO additions enabled stable propagation in Al/I_2O_5 composites by forming condensed Cu species that improved heat feedback.[9] Similarly, Si additives in $Al/KClO_4$ composites increased burn rate by increasing particle residence time on the burning surface, thereby enhancing heat feedback to the pre-heating zone.[10]

Because propagation reflects coupled chemistry-transport dynamics, many investigations have attempted to infer reaction kinetics and thermal properties of composites from spatial and temporal temperature measurements during combustion.[11] Classical approaches, such as embedding thermocouples directly within the reactive bed, have provided valuable insight into bulk heat transfer and reaction timing, but suffer from practical limitations for energetic composites: as thermocouples can perturb the sample, are difficult to deploy at the microscale, and cannot withstand the very high temperatures encountered in many thermite systems.[12] Noninvasive optical diagnostics provide an attractive alternative: For example, multi-color pyrometry under a gray body assumption has been widely applied for particle temperature measurements but is generally unapplicable at low temperatures due to reduced thermal emission.[13] Infrared (IR) thermography has been used to characterize pre-heating zones at lower temperatures. Cha *et al.* used infrared imaging to study how particle–interface morphology influences macroscopic burn rate and reported that improved reaction homogeneity lowers the reaction onset temperature and increases burn rate.[14]

In our previous study, we systematically investigated the effect of carbon fiber (CF) additive on the burn rate of six nanothermite composites.[15] We found that Al/MnO_2, Ti/MnO_2, and B/Bi_2O_3 composites produce *dispersed phased products* where burning particles detach from the burning surface. In these cases, adding CF *increased* the burn rate. High-speed microscopic imaging showed that the ejected burning particles were intercepted by the CF, holding them near the reaction front and thus, through a much increased residence time, significantly increased heat feedback and thus burn rate (and power). This mechanism has also been exploited in an aluminized ammonium perchlorate/hydroxyl-terminated polybutadiene (AP/HTPB) propellant to increase the burn rate, as well as in mesoparticle composites to modulate combustion behavior.[16,17] Conversely, when CF was added to composites that produce *continuous phase reaction* products that remain attached to the unburnt sample (B/MnO_2, B/Fe_2O_3, and B/Fe_3O_4), we observed a *reduction* in burn rate. In this case, the CF presumably acts to blead energy away from the reaction front to both the pre-heating and post-flame zones. Implying that an increase in thermal diffusivity was actually a detriment. Recent work has highlighted the importance of product morphology in controlling flame stability and combustion propagation in nanocomposites.[18] However, quantitative determination of the effective thermal transport properties during propagation remains challenging.

To test this hypothesis in this paper, we combine color camera imaging pyrometry and IR imaging to capture the combustion temperature profiles spanning the reaction zone and into the pre-heating zone. From these spatially resolved temperature profiles, we extracted both the flame temperature and the reaction initiation (ignition) temperature for samples with and without CF. The measured flame and initiation temperatures were comparable between CF doped and undoped samples, supporting the assertion that the low amount of CF additive is chemically inert with respect to the primary nanothermite chemistry, and that observed burn rate changes are dominated by thermal property alterations. We then fit the temperature profile in the pre-heating zone to solutions of the heat diffusion equation to extract effective thermal diffusivities. These diffusivities increased consistently with CF additive. Coupling these experimental diffusivities to transient heat transfer simulations reproduces the observed decrease in burn rate for the continuous phase systems, confirming that enhanced heat dissipation into the pre-heating zone is the primary driver of the CF-induced burn rate suppression. This work introduces a robust, noninvasive methodology for measuring full combustion temperature profiles in nanothermite composites and for extracting *in situ* thermal properties during reaction. The combined experimental-computational framework clarifies how nonreactive additives that alter transport properties (rather than chemistry) can produce qualitatively different effects depending on the morphology of reaction products. These findings provide design rules for tailoring propagation behavior in energetic composites through controlled microstructure and additive selection.

II. EXPERIMENTAL

A. Materials

Aluminum nanoparticles (Al, 100 nm, 92 wt. % active), boron nanoparticles (100 nm, 85 wt. % active), titanium nanoparticles (Ti, 30–50 nm, 75 wt. % active), manganese dioxide nanoparticles (MnO_2, 50 nm), and bismuth oxide nanoparticles (Bi_2O_3, 80 nm) were purchased from US Research Nanomaterials. Iron (III) oxide nanoparticles (Fe_2O_3, <50 nm) and iron (II, III) oxide nanoparticles (Fe_3O_4, <50 nm) were purchased from Sigma Aldrich. Carbon fiber [CF, Polyacrylonitrile (PAN)-based, diameter: 7 μm, length: 3 mm] was purchased from Composite Envisions. METHOCEL™ F4M hydroxypropyl methylcellulose (HPMC) and poly(vinylidene fluoride) (PVDF) were purchased from Dow Chemical Co. and Sigma Aldrich. *N*,*N*-dimethylformamide (DMF, 99.8%) was purchased from Fisher Scientific.

B. Direct writing ink preparation and nanothermite composite fabrication

Detailed direct writing ink compositions and samples fabrication procedure are described in our previous publications.[14,19] Briefly, 4 wt. % PVDF, 6 wt. % HPMC, and 90 wt. % of fuel and oxidizer nanoparticles at equivalence ratio ($\Phi = 1$) were mixed in DMF to form high loading inks and printed into free-stranding sticks. For samples with CF, an additional 2.5 wt. % CF was added to the inks and printed using the same process. After drying to remove solvent, the composites were cut into ~20 mm free-standing sticks with cross-sectional area of $\sim 1 \times 1$ mm^2.

FIG. 1. Experiment setup of the combustion tests. (Note: the combustion chamber was not shown and the objects were not drawn to scale.)

C. Combustion experiment system

The free-standing samples were taped on sapphire windows (330 μm, University Wafer, Inc.) at one end and mounted inside the testing chamber with the same sapphire window. The samples were ignited by a resistively heated nichrome wire (diameter: 250 μm, Ted Pella, Inc.) at the opposite terminus where the samples were mounted. All tests were performed in argon except B/Fe_3O_4 and B/Fe_3O_4/CF samples, which were tested in air since combustion could not propagate in argon. The combustion processes were imaged by a color camera and an infrared (IR) camera. The IR camera was positioned normal to the sample surface while the color was mounted above the IR camera at ~30° tilt (Fig. 1).

D. Color camera imaging, burn rate, and burning particle temperature measurement

The combustion processes of all samples were recorded by a color camera at a resolution of ~35 μm per pixel (Miro M1100, Vision Research, with AF Micro NIKKOR 105 mm lens, Nikon). The working distance between the lens and the sample was maintained at ~8 in. during pyrometry calibration and experiments to ensure consistent magnification and imaging conditions. Composites with dispersed phase products and continuous phase products were recorded at 5000 and 2000 frames per second, exposure time were set at 40 and 200 μs, respectively. Burn rates were calculated from the measured burn distance in the center region (~15 mm) divided by the burn time to eliminate edge effects. The color camera was calibrated using a blackbody source (Mikron M390) to enable its use as a three-color imaging pyrometer, as described in our previous work.[20,21] Visible emission was recorded by a Bayer-filtered detector (spectral response ~400–700 nm, RGB channel bandwidths of ~100 nm FWHM). Under the gray body assumption, ratio pyrometry from the RGB channels was used to evaluate the spatial and temporal temperatures by comparing the measured RGB intensity ratios with theoretical blackbody radiation, with an estimated uncertainty of ±200 K. Emission spectroscopy was performed to verify that no significant AlO or BO_2 molecular emissions were present within the wavelength range used for three-color pyrometry (supplementary material discussion). This method was limited to temperatures above 1000 K and could, therefore, only be applied to the reaction zone during nanothermite combustion.

E. Infrared camera imaging

To evaluate the lower temperature pre-heating zone, we employed an IR camera with spectral range from 3.0 to 5.4 μm and spatial resolution of ~30 μm per pixel (FAST M3K with 1× lens, Telops). The samples were imaged using three calibrated ranges to obtain the completed temperature profile (low range: 415–680 K, middle range: 571–1113 K, and high range: 716–1801 K, the manufacturer specified temperature accuracy is ±2% of the measured temperature). The exposure times were set at 20 μs and the frame rates were the same as color camera imaging. The temperature profile in each range was extracted along the centerline and frame averaged. The effective emissivity of nanothermite composites was estimated by fitting the temperature profile in the high range from the IR measurement to the color pyrometry results by 0.05 increments in emissivity value, and the effective emissivity was assumed to be temperature independent. The same value was then applied to the middle and low temperature ranges. The transmittance of a single sapphire window was measured as 88% by a spectrometer (Nicolet iS50R, Thermo Fisher) in the 3–5 μm wavelength range (Fig. S1 in the supplementary material), and the total transmittance is 77% for the optical system consists of two sapphire windows.

F. Burn rate simulation

A transient heat transfer model was implemented using the COMSOL Multiphysics 6.3 package to study the effect of thermal properties of products and reactants on the burn rate of composites with continuous phase products. The governing equation used to solve the transient temperature profile for the combustion wave was expressed as[22]

$$k\left(\frac{\partial^2 T}{\partial x^2}\right) + Q_{rxn} - Q_{conv} - Q_r = \frac{\partial T}{\partial t}\rho C_p, \quad (1)$$

where k is the thermal conductivity, ρ is the density, and C_p is the heat capacity. Q_{conv} and Q_r are the convection heat and radiation

heat loss to the ambient. Heat release from the reaction (Q_{rxn}) was defined as

$$T(\textit{local temperature}) > \textit{Reaction initiation temperature},$$
$$Q_{rxn} = \rho \Delta H A (1-\eta) \exp\left(-\frac{E_a}{RT}\right), \tag{2}$$
$$T < \textit{Reaction initiation temperature}, \; Q_{rxn} = 0,$$

where ΔH is the heat of reaction, A is the Arrhenius factor, η is the fraction of product phase, E_a is the activation energy, and R is the gas constant. The reaction was initiated by applying the ignition temperature ($T^* > \textit{Reaction initiation temperature}$) at right boundary, convection and radiation heat losses were included at the other boundaries.

To understand the relationships of the various parameters on propagation velocity, we nondimensionalize the problem with Ref. 23,

$$\dot{T} = \frac{T}{T^*}, \quad \dot{k} = \frac{k}{k^*}, \quad \dot{t} = \frac{t}{t^*}, \quad \dot{\Delta H} = \frac{\Delta H}{C_p T^*}, \quad \dot{x} = \frac{x}{x^*}, \quad \dot{E_a} = \frac{E_a}{RT^*}, \tag{3}$$

where k^* is the reference thermal conductivity and the characteristic time and length scales,

$$t^* = \frac{exp(\dot{E}_a)}{A}, \quad x^* = \sqrt{\frac{k^* t^*}{\rho C_p}}. \tag{4}$$

The governing equation (1) after nondimensionalization,

$$\dot{k}\left(\frac{\partial^2 \dot{T}}{\partial \dot{x}^2}\right) + \dot{Q_{rxn}} - \dot{Q_{conv}} - \dot{Q_r} = \frac{\partial \dot{T}}{\partial \dot{t}}, \tag{5}$$

where the nondimensional heat release from reaction ($\dot{Q_{rxn}}$) is given as

$$\dot{Q}_{rxn} = \dot{\Delta H} A t^* (1-\eta) \exp\left(-\frac{\dot{E}_a}{\dot{T}}\right). \tag{6}$$

The nondimensional heat transfer by convection ($\dot{Q_{conv}}$) and radiation heat loss ($\dot{Q_r}$) to ambient are

$$\dot{Q_{conv}} = \frac{h_{conv} t^* \left(\dot{T} - \dot{T_0}\right)}{\rho C_p}, \quad \dot{Q_r} = \frac{\sigma \varepsilon T^{*3} t^* \left(\dot{T}^4 - \dot{T_0}^4\right)}{\rho c_p}, \tag{7}$$

where $\dot{T_0}$ is the nondimensional ambient temperature, σ is the Stefan–Boltzmann constant, and ε is the effectivity emissivity determined experimentally. It should be noted that the purpose of the burn rate simulation is to evaluate the trends of how thermal property changes affect the burn rate of composites, but not to quantitatively reproduce the full experimental temperature profile or absolute burn rates as many fundamental parameters such as reaction rate are unknown. The model employs simplified one step reaction kinetics and does not account for complex nanothermite processes such as nanoparticle sintering phase transformation.

III. RESULTS AND DISCUSSION

A. Combustion temperature profile measurement

Three-color pyrometry is a reliable temperature probe for high temperatures (>1000 K), but thermal emission intensity drops rapidly with temperature decrease according to the Stefan–Boltzmann law. Consequently, extracting pre-heating zone profiles from visible wavelength pyrometry is difficult, necessitating moving to the IR to extend the temperature measurement below 1000 K. Although the nanothermite loading is 90 wt. % in the composites, the polymer matrix still generates gas during combustion. To prevent hot gas from obscuring the IR measurement,[24] the composites were taped to a sapphire window at the opposite end to the ignition point, thereby reducing interference from gas release. The rough surface of the composites ensured only loose contact with the sapphire window. The intrinsic burn rate of composites with different product morphology and samples with CF additive is plotted in Figs. 2(a) and 2(b). The burn rates of intrinsic samples and with CF showed the same morphology-dependent trends observed previously for free-standing samples (Table S1 in the supplementary material),[15] confirming that the sapphire windows do not influence burn rate. The high, uniform IR transmittance of sapphire in the mid-wave IR wavelength allowed temperature profile measurements with the IR camera, while also not affecting the visible ratio pyrometry results under gray body assumption. Figure 2(c) demonstrates the procedure used to obtain combustion temperature profile for B/MnO_2 composites. The solid (green) line represents the measurement from color pyrometry, and the scatter lines represent the IR measurement from different temperature ranges. The IR measurements were corrected for total transmittance (77%) along the light pass, and the effective emissivity was estimated by adjusting the emissivity with 0.05 increments until the IR profile at high temperature range showed the best match with the color pyrometry results. The cross-sectional images of samples showed that most of the CF remained embedded within the composites during the direct writing process.[15] Since the IR camera measures the surface radiation from the composites, the CF additive has minimal interference with the temperature measurement. The estimated effective emissivity was between 0.7 and 0.8 regardless of CF additive. The temperature profile can be divided into two regions for further analysis. The reaction zone (after 0 μm position) is defined to be where chemistry takes place, and results in the rapid temperature rise in this region. The pre-heating zone is located before the reaction zone (before 0 μm position), and it is assumed there is no chemical reaction, with the temperature profile reflecting heat transfer from the reaction zone. The combined combustion temperature profile in Fig. 2(c) shows an inflection point (at 0 μm position), determined from the departure of the semi-log plot of normalized temperature (Fig. S2 in the supplementary material).[25] This point represents the conceptual boundary between the pre-heating zone and the reaction zone during nanothermite propagation. The combined combustion temperature profile of other samples is plotted in Fig. S3 in the supplementary material.

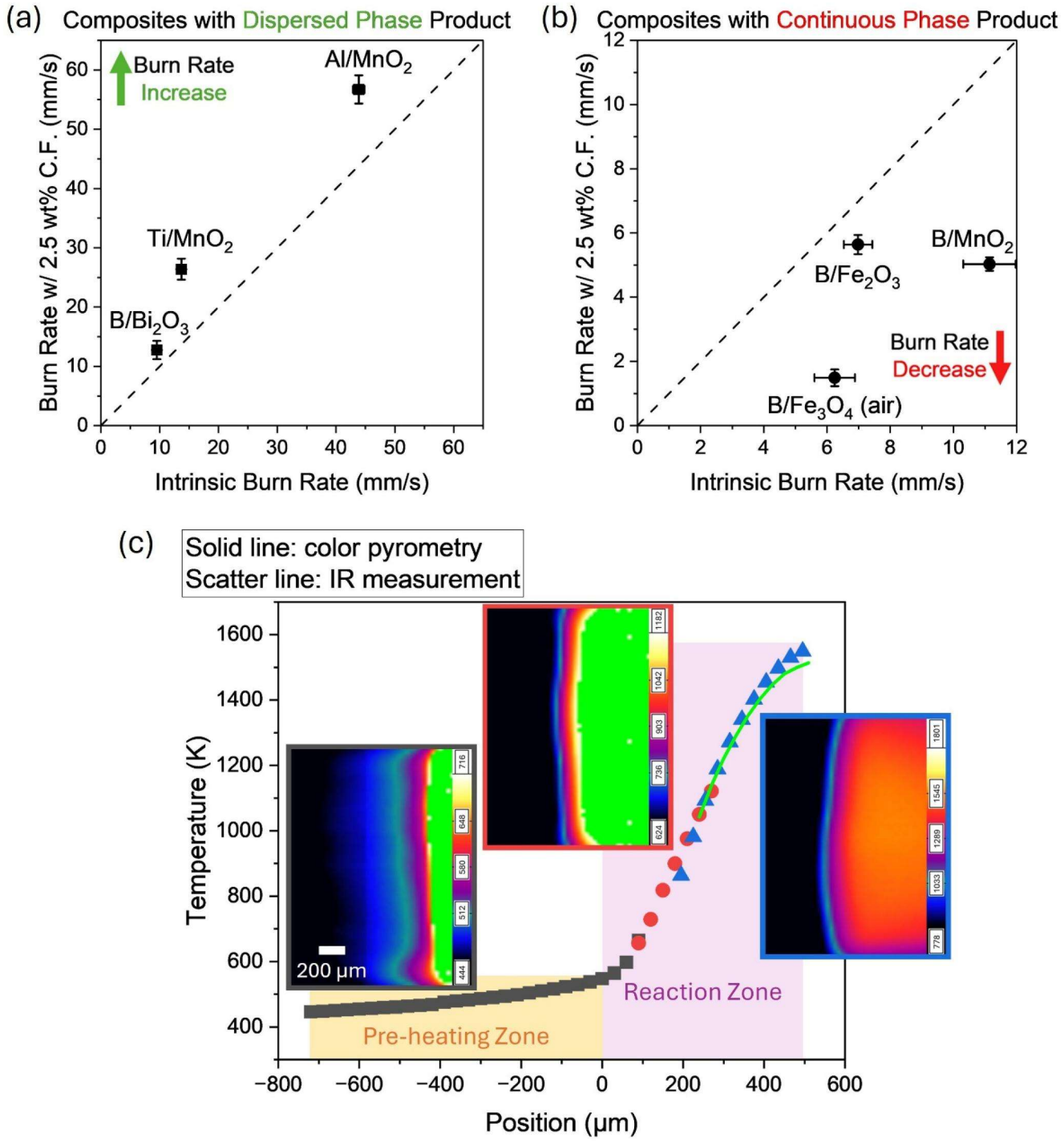

FIG. 2. Effect of burn rates change with CF addition. (a) Adding CF increases the burn rate of composites with dispersed phase products. (b) CF decreases the burn rate of composites with continuous phase products. Green and red annotations denote burn rate increase and burn rate decrease, respectively. Data points above the bisector correspond to increased burn rate, while data points below the bisector correspond to decreased burn rate. (Burn rates were measured using free-standing samples taped to sapphire windows for IR measurements.) (c) Combustion temperature profile of B/MnO_2 composites measured by color camera and IR camera. The combustion wave propagated from right to left.

B. Flame temperature and reaction initiation temperature

The flame temperature of the nanothermite composites was determined by color imaging pyrometry. Figure 3(a) shows Al/MnO_2 composites in left column as an example of composites with dispersed phase products along with its color pyrometry results below, the images in right column are composites with CF additive. B/MnO_2 results are shown in Fig. 3(b) to represent composites with continuous phase products. Figures 3(c) and 3(d) show results for flame temperatures for the dispersed and

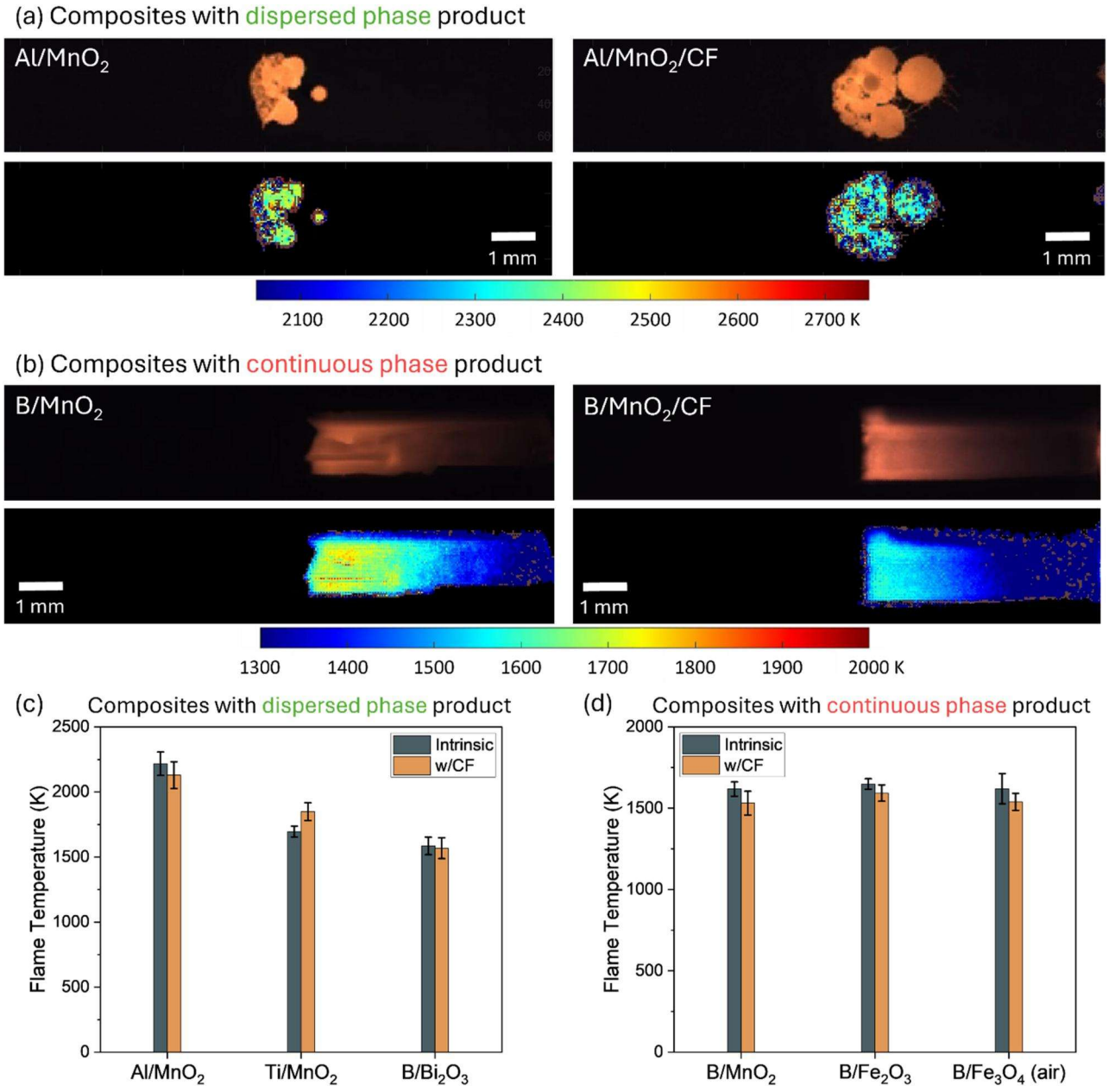

FIG. 3. (a) Color pyrometry results of Al/MnO_2 samples and with CF additive representing composites with dispersed phase products. (b) Color pyrometry results of composites with continuous phase products, example: B/MnO_2 and with CF addition. The top row shows the high-speed color camera images, and the bottom row shows the corresponding three-color pyrometry temperature maps. (c) Flame temperature of composites with dispersed phase products and (d) composites with continuous phase products. The propagation direction is from right to left.

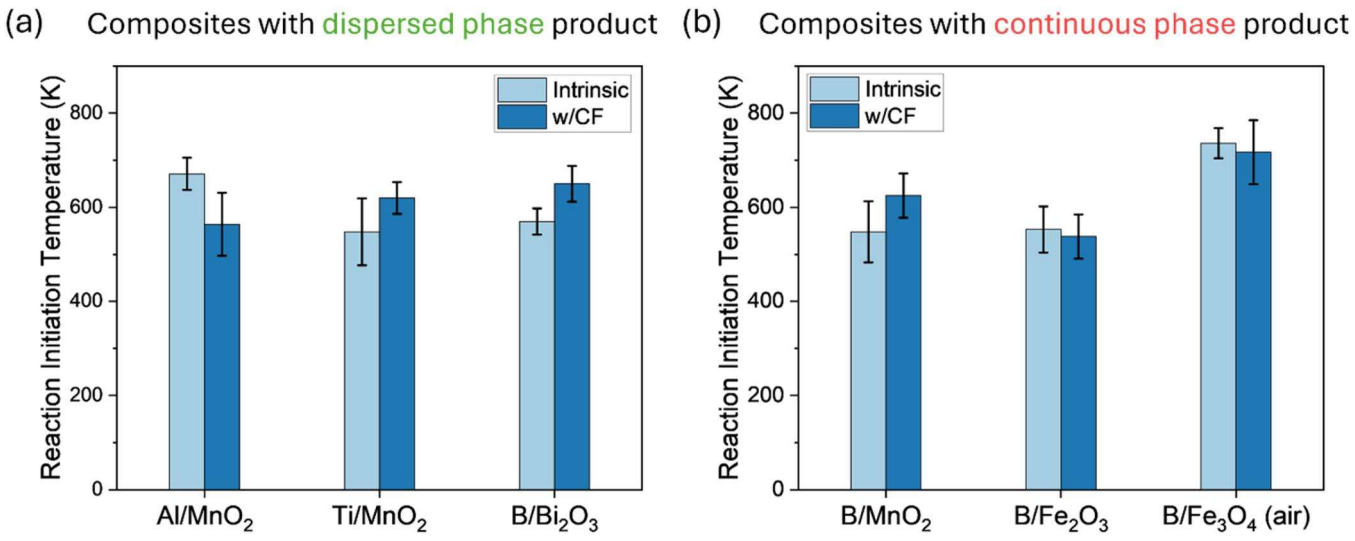

FIG. 4. Reaction initiation temperature of (a) composites with dispersed phase products and (b) samples with continuous phase products determined from temperature profile during combustion.

continuous phases, respectively. The flame temperature of composites with dispersed phase products were calculated as the mean of the particle temperatures, while for the composites with continuous phase products, the flame temperature was taken as the average of the maximum temperature along the axial profile during combustion. Pyrometry measurements of other composites are shown in Fig. S4 in the supplementary material. The key feature of these results is that while flame temperature differences exist due to changes in thermite composition, the addition of small amount of CF does not alter the flame temperature significantly regardless of phase of product, even though CF addition clearly manipulates the burn rate.

Since IR imaging extends the temperature profile into the pre-heating zone, the reaction initiation temperature can be defined as the temperature at the inflection point (an imaginary boundary between reaction zone and pre-heating zone) and is plotted in Fig. 4. The reaction initiation temperatures for intrinsic samples are comparable with CF doped samples and again support the conclusion that adding small amounts of CF does not significantly alter the intrinsic combustion process and heat release in the reaction zone.

C. Extracting thermal transport properties from the temperature profile

Since the flame temperature and reaction initiation temperature were not significantly affected by CF addition, we may conclude that the primary role of CF can be attributed to modifying thermal transport, specifically the effective thermal diffusivity of the composites. Under the assumption that heat release in the pre-heating zone is minimal, we can apply the heat diffusion equation [Eq. (8)],

$$\frac{dT}{dt} = \alpha_{eff}\left(\frac{d^2T}{dx^2}\right), \tag{8}$$

where α_{eff} is the effective thermal diffusivity of the sample in the pre-heating zone *in operando*. Since the burn rate (v) of samples were constant during combustion, Eq. (8) can be simplified by substituting $x = vt$ yielding Eq. (9),

$$\frac{dT}{dx} = \frac{\alpha_{eff}}{v}\left(\frac{d^2T}{dx^2}\right), \tag{9}$$

where v is the burn rate of composites shown in Figs. 2(a) and 2(b). $\frac{dT}{dx}$ and $\frac{d^2T}{dx^2}$ can be numerically evaluated by applying exponential fitting the measured temperature profile in the pre-heating zone [Fig. 5(a)]. The measured effective thermal diffusivities for intrinsic composites and samples with CF additive are plotted in Figs. 5(b) and 5(c) and clearly show that CF addition increases the effective thermal diffusivity as expected. The different increment in α_{eff} among different nanothermite composites may be influenced by differences in particles size, particle number density, and microstructure within the printed samples. We attribute the variation in the different increase in α_{eff} primarily to the differences in the interaction between burning particles and CF during combustion.[15] For example, Al burns as liquid droplets and can establish thermal contact with CF by Al–C bond formation.[26] In contrast, Ti particles show fractal morphology during combustion, while B particles were covered by a viscous liquid boron oxide layer at measured flame temperature which exhibits different contact characteristics with fibers.[27] These differences can influence how efficiently heat is transferred through the CF into the pre-heating zone during propagation. The increase is quite significant, especially given that CF addition is only 2.5 wt. %. Data for thermal properties, particularly nanoparticles in a packed form, are largely unavailable. The thermal diffusivity of different PAN-based CF is measured to be $\sim 2 \times 10^{-5}$ m^2/s[28] and of course higher than the thermal diffusivity of the polymers

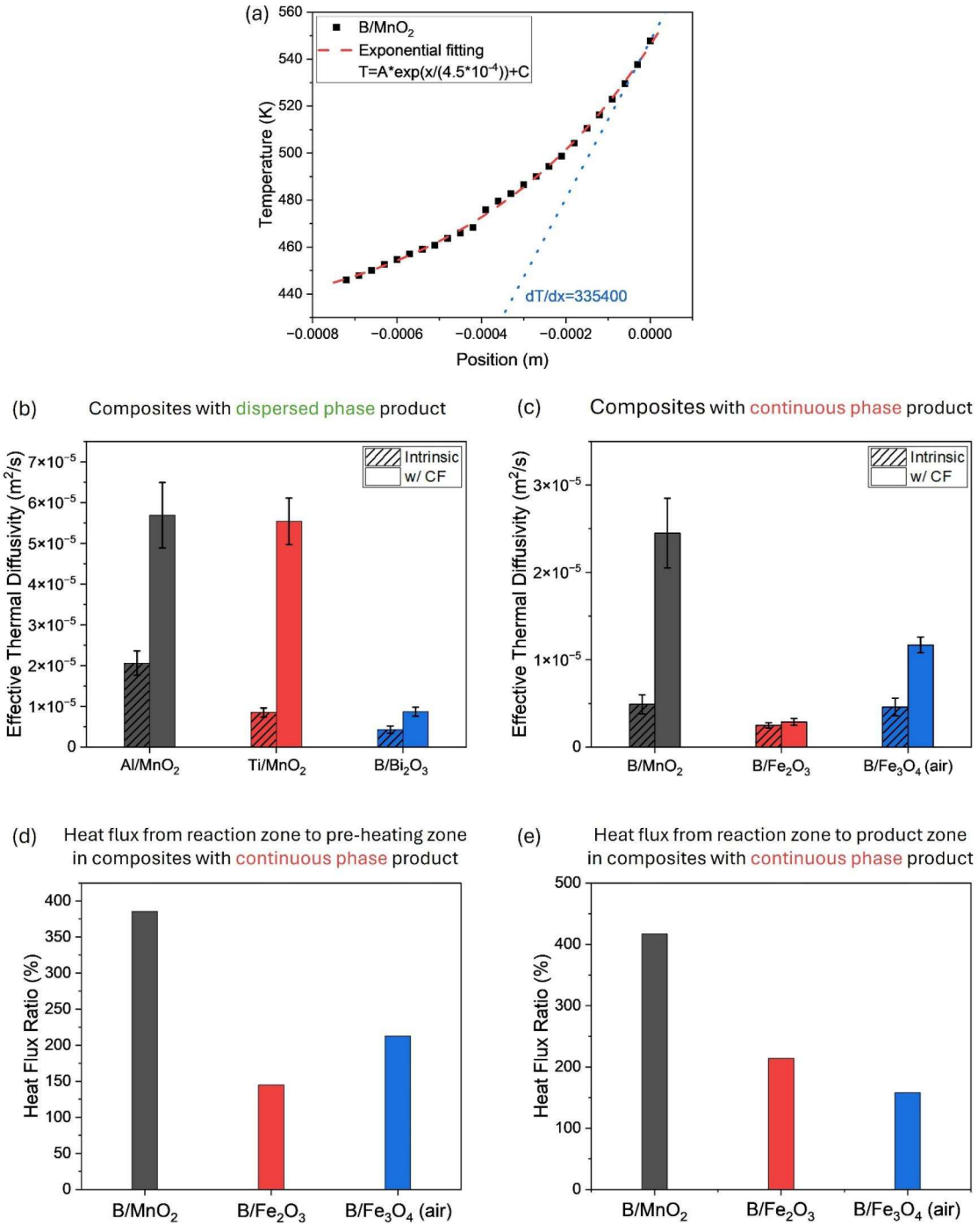

FIG. 5. (a) Example of extracting effective thermal diffusivity from the pre-heating zone temperature profile for the B/MnO_2 sample. Dashed line represents the exponential fit, $T = A * \exp(\frac{x}{t}) + C$, where A and t are fitting parameters and C was fixed to the ambient temperature and dotted line is the tangent line at the reaction initiation temperature. The propagation direction is from right to left. (b) Effective thermal diffusivity of composites with dispersed phase products in the pre-heating zone. (c) Effective thermal diffusivity of samples with continuous phase products in the pre-heating zone. Additional data at multiple CF loading for the representative dispersed phase product system and the continuous phase product system are plotted in Fig. S7 in the supplementary material. (d) Heat flux ratios increase by CF from reaction zone to pre-heating zone in composites with continuous phase products. (e) Heat flux ratios increase from reaction zone to product zone by CF additive.

and oxidizers used in this study when based on bulk material. The thermal diffusivities of bulk metal are $\sim 10^{-5}$ m^2/s; however, the metal nanoparticles have a native oxide shell surrounding the metal core, whose thermal diffusivities are an order of magnitude lower than bulk metal and CF. (Bulk values were listed in Table S2 in the supplementary material.)[29] Consequently, the high-aspect-ratio CF which are aligned parallel to the propagation direction during printing can form thermal conductive pathways and increase α_{eff} effectively.[30,31] These values are obtained in operando from IR measurements at elevated temperatures and represent effective properties during combustion. As such, they are not directly comparable to values obtained from steady states.

Once the thermal diffusivity is determined, we can now reevaluate the thermal profile to estimate the heat flux (q) from reaction to pre-heating zone and can be calculated from the temperature profile at the boundary by Eq. (10),

$$q = k\frac{dT}{dx} = \alpha_{eff}\rho C_p \frac{dT}{dx}, \tag{10}$$

where ρ and C_p are density and specific heat capacity of the nanothermite composites, respectively. In addition, $\frac{dT}{dx}$ is the slope of the tangent line [dotted line in Fig. 5(a)] at the reaction initiation point. Since only small amounts of CF were used as an additive, we assume the specific heat capacity of the composites was constant, and the density of the composites measured by dividing the mass of the composites by the volume in our previous study also shows no significant change by small amount of CF additive.[15] We define a heat flux ratio to assess the amplification effect of CF addition by Eq. (11),

$$Heat\ flux\ ratio = \frac{q_{w/CF}}{q_{intrinsic}} * 100. \tag{11}$$

The heat flux ratios all show an increase upon CF addition regardless of the nature of the product morphology [Figs. 5(d) and S5 in the supplementary material]. For composites with continuous phase product, the effectivity thermal diffusivity in the product zone can also be calculated by Eq. (4) and plotted in Fig. S6 in the supplementary material. Since the CF structure is thermally stable at the measured flame temperature and remains embedded in the product, the effective thermal diffusivities in the product zone also show an increase.[16,17] Therefore, the heat fluxes from the reaction zone to the product zone for composites with continuous phase product can also be calculated using Eq. (5) and the results show that the heat flux increases with CF addition [Fig. 5(e)]. With all the heat fluxes acquired, we can comment on the mechanism by which CF addition can actually decrease the burn rate of composites with a continuous phase product. Since the temperature in the reaction zone remains unchanged by small amount of CF addition, increasing thermal diffusivity apparently leads to greater energy dissipation into both the pre-heating and product zone.[32,33] For composites with dispersed phase products, the CF increases the residence time of agglomerates at or on the burning surface by intercepting the ejected particles increasing heat feedback to reaction front.

D. Burn rate simulation

To further explore the issues raised by the experiments on the role of thermal transport on flame propagation, we perform COMSOL simulations. To parameterize the problem systematically, we define $\Pi = \frac{\dot{k}_r}{\dot{k}_p}$ as the ratio of the dimensionless thermal conductivity of reactant over product. For this simulation, $\dot{k}_r$ is varied from 1 to 10 reflecting the experimental observed increase in effective thermal diffusivity in the pre-heating zone by CF additive, while $\dot{k}_p$ was kept constant at 1. Figure 6(a) shows simulated dimensionless temperature profile under steady propagation for different values of Π. With increasing Π (i.e., increasing $\dot{k}_r$ relative to $\dot{k}_p$), the temperature profile widens in the pre-heating zone (below reaction initiation temperature). The dimensionless burn rates ($\dot{v}_s = v_s t^*/x^*$) are the positional evolution of the reaction initiation point and are plotted in Fig. 6(b) as a function of Π along with the dimensionless heat flux $\left(\dot{q}_{diff} = \dot{k}_r * \frac{d\dot{T}}{d\dot{x}}\right)$ at reaction initiation point. The simulated dimensionless burn rate decreases with increasing $\dot{k}_r$ while the dimensionless heat flux to the pre-heating zone also increases. *This is consistent with our experimental result that adding carbon fiber to a continuous phase product increases the heat flux but decreases the burn rate* [Figs. 5(c) and 5(d)]. The effect of exothermic heat release is shown in Fig. S6(a) in the supplementary material. For the same value of Π, increasing $\Delta\dot{H}$ increases the burn rate.

Because the burn rate is governed by the interplay of reaction generated heat release, and thermal transport to the pre-heating zone, it is instructive to evaluate a thermal Damköhler number (thermal Da) defined as

$$Thermal\ Da = \frac{\dot{q}_{rxn}}{\dot{q}_{diff}} = \frac{\dot{v}_s * \Delta\dot{H}}{\dot{q}_{diff}}. \tag{12}$$

In this case, the chemical reaction rate is essentially the dimensionless burn rate ($\dot{v}_s$) from which the heat release rate is evaluated for the numerator. The dimensionless heat flux in the denominator is evaluated as the heat flux at the pre-heat boundary. The calculated thermal Da number > 1 for all simulated conditions indicated that the burn rate is thermal transport limited. This conclusion was further supported by analyzing the temperature gradient obtained from the simulated temperature profile [Fig. S8(b) in the supplementary material]. Since there was no heat release below reaction initiation temperature in the simulation (corresponding to no reaction taking place in pre-heating zone), the temperature gradient calculated from the slope of the tangent line at reaction initiation temperature is nearly constant regardless of $\Delta\dot{H}$ with same $\dot{k}_r$. As thermal Da number decreases, the heat flux into the pre-heating zone becomes increasingly comparable to reaction heat generation and can be inferred from the sensitivity of burn rate. Sensitivity analysis was performed for $\dot{k}_r$ and $\dot{v}_s$ by Eq. (13),

$$S = \frac{d\ln(\dot{v}_s)}{d\ln\left(\dot{k}_r\right)}. \tag{13}$$

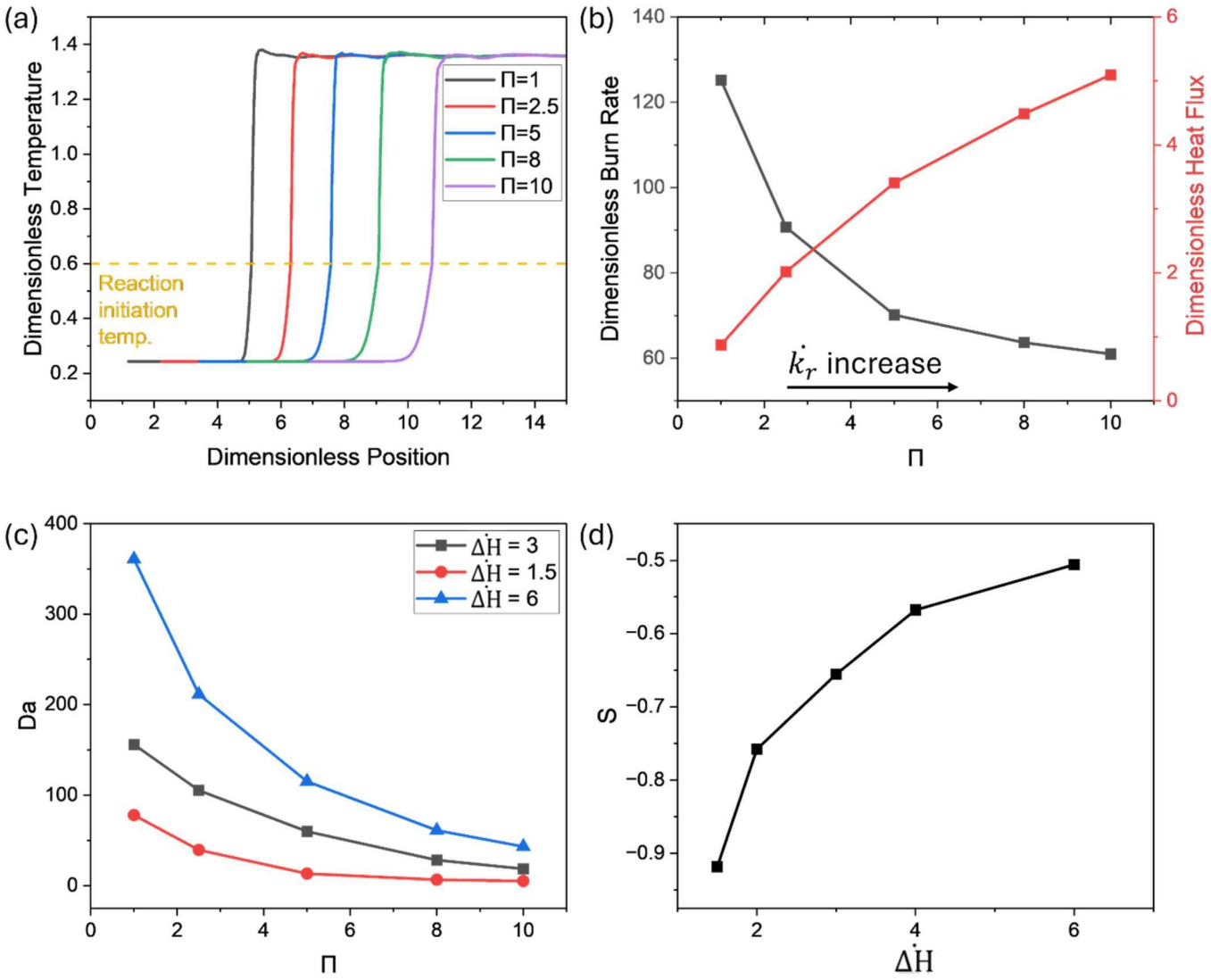

FIG. 6. (a) Simulated temperature profiles with different Π (dimensionless thermal conductivity parameter) at steady propagation stage. Profiles were displaced for demonstration. (b) Simulated dimensionless burn rate and heat flux with different Π ($\Delta\dot{H}$ (dimensionless heat of reaction) = 3). (c) Da (Thermal Damköhler number) with different Π with different $\Delta\dot{H}$. (d) Absolute value of sensitivity coefficient (S) increases with decreasing $\Delta\dot{H}$.

The evaluated sensitivity coefficients obtained from the linear fitting of $\ln(\dot{v}_s)$ and $\ln\left(\dot{k}_r\right)$ with different $\Delta\dot{H}$ were plotted in Fig. 6(d). The absolute value of sensitivity coefficients increases with decreasing $\Delta\dot{H}$ suggesting that burn rate becomes more sensitive to thermal conductivity of reactant in systems with lower reaction enthalpy, corresponds with the thermal Da number decreasing with $\Delta\dot{H}$ indicating that heat feedback become more dominating with relative insufficient heat release in reaction zone. While the simulations are not intended to fully replicated the measured temperature profiles, it demonstrated that increased heat dissipation can reduce the burn rate in composites with condensed products, supporting the experientially observed behavior.

These results reinforce the experimental findings: in continuous phase products systems, CF increases effective thermal diffusivity, leading to greater heat loss and slower burn rate. In composites with dispersed phase products, additional energy feedback from burning agglomerates compensates for the enhanced diffusivity, resulting in increased burn rate. Together, experiments and simulations provide a coherent mechanistic framework for understanding how thermal transport and kinetics can be modulated by additives such as CF influences nanothermite composite burn rate.

IV. CONCLUSIONS

This study establishes a method to obtain a complete combustion temperature profile of nanothermite composites by combining color imaging pyrometry and infrared imaging. The measured temperature profiles revealed a clear transition between these zones and allowed extraction of thermal properties from preheating zone in operando. Measurements on six different nanothermite composites, which were classified based on the combustion product morphology observed by real-time imaging into dispersed phase products (Al/MnO_2, Ti/MnO_2, and B/Bi_2O_3) and continuous phase products (B/MnO_2, B/Fe_2O_3, and B/Fe_3O_4) showed that adding CF has no significant effect on the flame temperature and reaction initiation temperature of composites, confirming that small amount of CF additive is chemically inert to the thermite reaction. However, CF consistently increases the effective thermal diffusivity of the composites. For composites with continuous phase products, this enhanced thermal transport increases energy dissipation into the pre-heating and product zones and decreases the burn rate. While for samples with dispersed phase products, CF intercept the ejected particles from the burning surface and increase the residence time of burning agglomerates, leading to faster propagation. Simulations replicating the experimental conditions reproduce the observed burn rate trends with CF addition, confirming that heat feedback plays a key role in the propagation of nanothermite composites. This study provides a novel method to extract thermal diffusivity and heat flux from combustion temperature profile and demonstrates the modulation of burn rate of nanothermite composites through manipulating the heat transfer during propagation.

SUPPLEMENTARY MATERIAL

The supplementary material includes more details on experimental configuration and calibration. Temperature profiles for all compositions and tabulated values for burn rate and extracted thermal diffusivities.

ACKNOWLEDGMENTS

This research was supported by the Department of Defense, Defense Threat Reduction Agency (DTRA) under the MSEE URA (Grant HDTRA1-20-2-0001) and the Army Research Office through award W911NF-22-2-0169.

AUTHOR DECLARATIONS

Conflict of Interest

The authors have no conflicts to disclose.

Author Contributions

Keren Shi: Data curation (lead); Formal analysis (lead); Visualization (lead); Writing – original draft (lead). **Yujie Wang**: Data curation (equal); Writing – review & editing (supporting). **Michael R. Zachariah**: Conceptualization (equal); Funding acquisition (equal); Investigation (equal); Methodology (equal); Project administration (lead); Resources (lead); Supervision (lead); Writing – review & editing (equal).

DATA AVAILABILITY

The data that support the findings of this study are available from the corresponding author upon reasonable request.

REFERENCES

[1]M. Zaky, A. Elbeih, and T. Elshenawy, "Review of nano-thermites; a pathway to enhanced energetic materials," Cent. Eur. J. Energy Mater. **18**, 63–85 (2021).
[2]B. Khasainov, M. Comet, B. Veyssiere, and D. Spitzer, "Comparison of performance of fast-reacting nanothermites and primary explosives," Propell. Explos. Pyrotech. **42**, 754–772 (2017).
[3]M. Polis, A. Stolarczyk, K. Glosz, and T. Jarosz, "Quo vadis, nanothermite? A review of recent progress," Materials **15**, 3215 (2022).
[4]C. R. Kachelmyer, A. Varma, A. S. Rogachev, and A. E. Sytschev, "Influence of reaction mixture porosity on the effective kinetics of gasless combustion synthesis," Ind. Eng. Chem. Res. **37**, 2246–2249 (1998).
[5]H. Wang, P. Biswas, and M. R. Zachariah, "Direct imaging and simulation of the interface reaction of metal/metal oxide nanoparticle laminates," J. Phys. Chem. C **126**, 8684–8691 (2022).
[6]L. Marín, C. E. Nanayakkara, J.-F. Veyan, B. Warot-Fonrose, S. Joulie, A. Estève, C. Tenailleau, Y. J. Chabal, and C. Rossi, "Enhancing the reactivity of Al/CuO nanolaminates by Cu incorporation at the interfaces," ACS Appl. Mater. Interfaces **7**, 11713–11718 (2015).
[7]H. Wang, Y. Wang, M. Garg, J. S. Moore, and M. R. Zachariah, "Unzipping polymers significantly enhance energy flux of aluminized composites," Combust. Flame **244**, 112242 (2022).
[8]G. C. Egan and M. R. Zachariah, "Commentary on the heat transfer mechanisms controlling propagation in nanothermites," Combust. Flame **162**, 2959–2961 (2015).
[9]D. J. Kline, Z. Alibay, M. C. Rehwoldt, A. Idrogo-Lam, S. G. Hamilton, P. Biswas, F. Xu, and M. R. Zachariah, "Experimental observation of the heat transfer mechanisms that drive propagation in additively manufactured energetic materials," Combust. Flame **215**, 417–424 (2020).
[10]Y. Wang, F. Xu, G. Issac Paul, E. Vidales Pasos, K. Shi, B. Wagner, L. Mangolini, and M. R. Zachariah, "Role of surface tension on heat feedback and power from energetic composites," ACS Appl. Mater. Interfaces **16**, 42100–42108 (2024).
[11]A. S. Mukasyan and C. E. Shuck, "Kinetics of SHS reactions: A review," Int. J Self-Propag. High-Temp. Synth. **26**, 145–165 (2017).
[12]T. Boddington, P. G. Laye, J. Tipping, and D. Whalley, "Kinetic analysis of temperature profiles of pyrotechnic systems," Combust. Flame **63**, 359–368 (1986).
[13]D. J. Kline, M. C. Rehwoldt, J. B. DeLisio, S. C. Barron, H. Wang, Z. Alibay, J. C. Rodriguez, G. M. Fritz, and M. R. Zachariah, "In-operando thermophysical properties and kinetics measurements of Al-Zr-C composites," Combust. Flame **228**, 250–258 (2021).
[14]B. Cha, A. Wang, S. Kim, J.-P. Hickey, S. Deng, and J. Z. Wen, "Microstructural thermal zones in reaction of nanoenergetics," ACS Appl. Mater. Interfaces **16**, 66099 (2024).
[15]K. Shi, Y. Wang, G. I. Paul, and M. R. Zachariah, "The influence of heat feedback and thermal conductivity on the burn rate of thermite composites," Combust. Flame **269**, 113593 (2024).
[16]H. Wang, E. Hagen, K. Shi, S. Herrera, F. Xu, and M. R. Zachariah, "Carbon fibers as additives to engineer agglomeration and propagation of aluminized propellants," Chem. Eng. J. **460**, 141653 (2023).
[17]Y. Wang, M. Chowdhury, Y. Zhou, G. Issac Paul, K. Shi, and M. R. Zachariah, "Oscillating-to-continuous combustion transition in mesoparticle composites through manipulation of heat feedback," Adv. Funct. Mater. **34**, 2406722 (2024).
[18]S. Kim, A. Wang, J. Z. Wen, and S. Deng, "Combustion waves and flame stability in nanocomposites," ACS Nano **19**, 31790–31798 (2025).

[19]J. Shen, H. Wang, D. J. Kline, Y. Yang, X. Wang, M. Rehwoldt, T. Wu, S. Holdren, and M. R. Zachariah, "Combustion of 3D printed 90 wt. % loading reinforced nanothermite," Combust. Flame **215**, 86–92 (2020).
[20]H. Wang, B. Julien, D. J. Kline, Z. Alibay, M. C. Rehwoldt, C. Rossi, and M. R. Zachariah, "Probing the reaction front of nanolaminates at ∼μs time and ∼μm spatial resolution," J. Phys. Chem. C **124**(25), 13679–13687 (2020).
[21]R. J. Jacob, D. J. Kline, and M. R. Zachariah, "High speed 2-dimensional temperature measurements of nanothermite composites: Probing thermal vs. gas generation effects," J. Appl. Phys. **123**, 115902 (2018).
[22]C.-L. Yeh, C.-C. Chou, and P.-W. Hwang, "Experimental and numerical studies on self-propagating high-temperature synthesis of Ta_5Si_3 intermetallics," Metals **5**, 1580–1590 (2015).
[23]M. Ballas, H. Song, and O. J. Ilegbusi, "Effect of thermal conductivity on reaction front propagation during combustion synthesis of intermetalics," J. Mater. Sci. **41**, 4169–4177 (2006).
[24]J. M. Densmore, K. T. Sullivan, and A. E. Gash, "Thermal imaging of thermite flame propagation," Report No. LLNL-JRNL-648519 (Lawrence Livermore National Laboratories, Livermore, CA, 2014).
[25]K. K. Kuo and R. Acharya, *Applications of Turbulent and Multiphase Combustion*, 1st ed. (Wiley, 2012).
[26]Y. Zhou and M. R. Zachariah, "Molecular dynamics study on the capture of aluminum particles by carbon fibers during the propagation of aluminum-based energetics," Energy Fuel **38**(10), 8992–9000 (2024).
[27]Y. Wang, E. Hagen, P. Biswas, H. Wang, and M. R. Zachariah, "Imaging the combustion characteristics of Al, B, and Ti composites," Combust. Flame **252**, 112747 (2023).
[28]W. Ohlhorst, L. Vaughn, and O. Ransone, "Thermal conductivity database of various structural carbon-carbon composite materials," NASA Technical Memorandum 4784 (1997).
[29]K. Bartsch, B. Bossen, W. Chaudhary, M. Landry, and D. Herzog, "Thermal conductivity of Ti-6Al-4V in laser powder bed fusion," Front. Mech. Eng. **8**, 830104 (2022).
[30]Y.-J. Kwon, J.-B. Park, Y.-P. Jeon, J.-Y. Hong, H.-S. Park, and J.-U. Lee, "A review of polymer composites based on carbon fillers for thermal management applications: Design, preparation, and properties," Polymers **13**(8), 1312 (2021).
[31]G. Lian, C.-C. Tuan, L. Li, S. Jiao, Q. Wang, K.-S. Moon, D. Cui, and C.-P. Wong, "Vertically aligned and interconnected graphene networks for high thermal conductivity of epoxy composites with ultralow loading," Chem. Mater. **28**(17), 6096–6104 (2016).
[32]M. Kobashi, D. Ichioka, and N. Kanetake, "Combustion synthesis of porous TiC/Ti composite by a self-propagating mode," Materials **3**, 3939–3947 (2010).
[33]Z. A. Munir and U. Anselmi-Tamburini, "Self-propagating exothermic reactions: The synthesis of high-temperature materials by combustion," Mater. Sci. Rep. **3**, 277–365 (1989).